

# Evidence of topological superconductivity in planar Josephson junctions

Antonio Fornieri<sup>1,10</sup>, Alexander M. Whiticar<sup>1,10</sup>, F. Setiawan<sup>2</sup>, Elías Portolés<sup>1</sup>, Asbjørn C. C. Drachmann<sup>1</sup>, Anna Keselman<sup>3</sup>, Sergei Gronin<sup>4,5</sup>, Candice Thomas<sup>4,5</sup>, Tian Wang<sup>4,5</sup>, Ray Kallagher<sup>4,5</sup>, Geoffrey C. Gardner<sup>4,5</sup>, Erez Berg<sup>2,6</sup>, Michael J. Manfra<sup>4,5,7,8</sup>, Ady Stern<sup>6</sup>, Charles M. Marcus<sup>1\*</sup> & Fabrizio Nichele<sup>1,9\*</sup>

**Majorana zero modes—quasiparticle states localized at the boundaries of topological superconductors—are expected to be ideal building blocks for fault-tolerant quantum computing<sup>1,2</sup>. Several observations of zero-bias conductance peaks measured by tunnelling spectroscopy above a critical magnetic field have been reported as experimental indications of Majorana zero modes in superconductor–semiconductor nanowires<sup>3–8</sup>. On the other hand, two-dimensional systems offer the alternative approach of confining Majorana channels within planar Josephson junctions, in which the phase difference  $\varphi$  between the superconducting leads represents an additional tuning knob that is predicted to drive the system into the topological phase at lower magnetic fields than for a system without phase bias<sup>9,10</sup>. Here we report the observation of phase-dependent zero-bias conductance peaks measured by tunnelling spectroscopy at the end of Josephson junctions realized on a heterostructure consisting of aluminium on indium arsenide. Biasing the junction to  $\varphi \approx \pi$  reduces the critical field at which the zero-bias peak appears, with respect to  $\varphi = 0$ . The phase and magnetic-field dependence of the zero-energy states is consistent with a model of Majorana zero modes in finite-size Josephson junctions. As well as providing experimental evidence of phase-tuned topological superconductivity, our devices are compatible with superconducting quantum electrodynamics architectures<sup>11</sup> and are scalable to the complex geometries needed for topological quantum computing<sup>9,12,13</sup>.**

The Josephson junctions (JJs) studied in this work were fabricated from a planar heterostructure comprising a thin Al layer epitaxially covering a high-mobility InAs two-dimensional electron gas (2DEG)<sup>14</sup>. As a consequence of the highly transparent superconductor–semiconductor interface<sup>15</sup>, a hard superconducting gap is induced in the InAs layer<sup>16,17</sup>. Selectively removing an Al stripe of width  $W_1$  and length  $L_1$  defines a normal InAs region, laterally contacted by superconducting leads, as shown in Fig. 1a. Superconducting gaps  $\Delta_{\text{exp}}(\pm i\varphi/2)$ , opening below the Al planes on the right-hand and left-hand sides<sup>18,19</sup>, respectively, confine low-energy quasiparticles within the normal InAs channel. Owing to the strong spin–orbit interaction in InAs (ref. <sup>14</sup>), together with the lateral confinement, the JJ of Fig. 1a is predicted to undergo a topological transition at high magnetic field  $B_{\parallel}$  parallel to the junction<sup>9</sup>, with Majorana modes isolated from the continuum forming at the end points (crosses in Fig. 1a), similarly to conventional nanowires<sup>20,21</sup>. Most strikingly, phase control offers an additional tuning parameter to enter the topological regime that has not been explored so far. Biasing the JJ to  $\varphi = \pi$  has been predicted to reduce the critical magnetic field of the topological transition, and to enlarge its phase boundaries in chemical potential<sup>10</sup>.

Here we investigate planar JJs such as that in Fig. 1a as a function of  $B_{\parallel}$ , chemical potential  $\mu$  and phase difference  $\varphi$ . Phase biasing is obtained by embedding the JJ in a direct-current superconducting

quantum interference device (d.c. SQUID) threaded by a magnetic flux<sup>22</sup>. A robust zero-bias peak (ZBP) exhibiting strong dependence on  $\varphi$  is measured by tunnelling spectroscopy using a laterally coupled quantum point contact (QPC), as schematically shown in Fig. 1a. The ZBP behaviour is consistent with a Majorana mode in a finite-size topological JJ (see Extended Data Figs. 1, 2).

Figure 1b shows a schematic of our device, which consists of a three-terminal asymmetric SQUID with two JJs, labelled 1 and 2, and a tunnelling probe coupling to a normal lead on the top end of JJ1. Figure 1c shows an electron micrograph in the surroundings of JJ1. The junctions are characterized by Josephson critical currents  $I_{c,2} > I_{c,1}$ , such that the phase difference  $\varphi$  across JJ1 can be tuned from 0 to  $\sim \pi$  by threading the SQUID loop with a magnetic flux  $\Phi$  (generated by the out-of-plane field  $B_{\perp}$ ) varying from 0 to  $\Phi_0/2$ , where  $\Phi_0 = h/2e$  is the superconducting flux quantum ( $e$  is the electron charge and  $h$  the Planck constant). The SQUID is laterally connected to two superconducting leads that serve as ground and enable measurement of the Josephson critical current of the interferometer (see Extended Data Figs. 9 and 10). The SQUID loop is obtained by a combination of deep wet etching on the semiconductor heterostructure and selective wet etching of the top Al layer. A  $\text{HfO}_2$  dielectric layer is deposited over the entire sample for gate isolation, followed by lift-off of the Ti/Au gate structures. Top gates  $V_1$  and  $V_2$  control the chemical potential in JJ1 and JJ2, respectively. Split gates deposited at the top end of JJ1 form a QPC. In the tunnelling regime, the QPC serves as a spectroscopic probe revealing the local density of states of JJ1. The uppermost gate extends between the QPC gates and helps to define a sharp tunnel barrier when operated at a voltage  $V_{\text{top}} \approx 0$ . To ensure a hard superconducting gap in high parallel fields, the QPC gates additionally confine the 2DEG beneath the narrow Al leads<sup>6,7</sup> (see Fig. 1c). We present data for a device with  $W_1 = 80$ ,  $W_2 = 40$  nm,  $L_1 = 1.6$   $\mu\text{m}$  and  $L_2 = 5$   $\mu\text{m}$ . The width of the superconducting leads is  $W_{S1} = W_{S2} = 160$  nm for both JJs, and the SQUID loop area is approximately 8  $\mu\text{m}^2$ . Data were reproduced for two additional devices with  $W_1 = 80$  nm and 120 nm respectively (other dimensions are the same as before) and are presented in Extended Data Figs. 5, 7 and 8. Differential conductance  $G$  was measured in a four-terminal configuration by standard a.c. lock-in techniques in a dilution refrigerator with an electron base temperature of about 40 mK.

Figure 2a shows  $G$  as a function of the bias voltage  $V_{\text{sd}}$  and  $\Phi$  at  $B_{\parallel} = 0$ . The induced superconducting gap  $\Delta(\Phi = 0) \approx 150$   $\mu\text{eV}$  periodically oscillates as a function of  $\Phi$  and is reduced by about 50% at  $\Phi = (2n + 1)\Phi_0/2$ , where  $n$  is an integer. This behaviour indicates phase-coherent transport through JJ1 generated by Andreev reflection processes<sup>23,24</sup> at the interfaces between the bare 2DEG and the proximitized leads. The flux modulation of the whole continuum of states outside the gap is expected for JJs with narrow superconducting leads ( $W_{S1} \ll \xi_s$ , where  $\xi_s = \hbar v_F / \pi \Delta \approx 1.5$   $\mu\text{m}$  is the superconducting

<sup>1</sup>Center for Quantum Devices, Niels Bohr Institute, University of Copenhagen and Microsoft Quantum Lab Copenhagen, Copenhagen, Denmark. <sup>2</sup>James Franck Institute, The University of Chicago, Chicago, IL, USA. <sup>3</sup>Station Q, Microsoft Research, Santa Barbara, CA, USA. <sup>4</sup>Department of Physics and Astronomy and Microsoft Quantum Lab Purdue, Purdue University, West Lafayette, IN, USA. <sup>5</sup>Birck Nanotechnology Center, Purdue University, West Lafayette, IN, USA. <sup>6</sup>Department of Condensed Matter Physics, Weizmann Institute of Science, Rehovot, Israel. <sup>7</sup>School of Materials Engineering, Purdue University, West Lafayette, IN, USA. <sup>8</sup>School of Electrical and Computer Engineering, Purdue University, West Lafayette, IN, USA. <sup>9</sup>Present address: IBM Research—Zurich, Rüschlikon, Switzerland. <sup>10</sup>These authors contributed equally: Antonio Fornieri, Alexander M. Whiticar. \*e-mail: marcus@nbi.ku.dk; fni@ibm.zurich.com

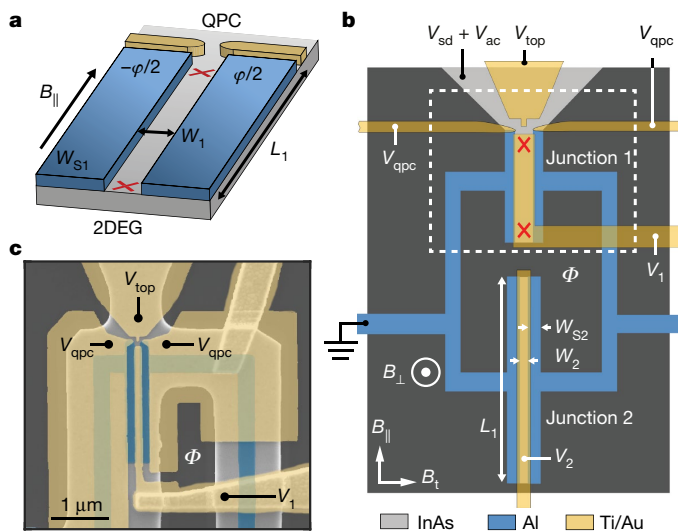


**Fig. 1 | Topological Josephson junction.** **a**, Schematic of a planar JJ formed by two epitaxial superconducting layers (represented in blue) covering a 2DEG with strong spin-orbit interaction (grey). A 1D channel, defined between the superconducting leads, can be tuned into the topological regime with Majorana modes (red crosses) at its ends by the parallel field  $B_{||}$ , the 2DEG chemical potential  $\mu$  and the phase difference between the superconductors  $\varphi$ . Majorana modes can be probed in tunnelling spectroscopy using a QPC located at one end of the JJ. **b**, Schematic of the measured device (not to scale) consisting of a superconducting loop interrupted by two JJs (labelled 1 and 2) in parallel. The interferometer is formed by InAs 2DEG (light grey) and epitaxial Al (blue). Five Ti/Au gates (yellow) allow independent tuning of the chemical potential in JJ1 (gate voltage  $V_1$ ), the chemical potential in JJ2 ( $V_2$ ) and the transmission of a tunnel barrier at the top end of JJ1 (with gate voltages  $V_{qpc}$  and  $V_{top}$ ). The applied a.c. and d.c. bias voltages ( $V_{ac}$  and  $V_{sd}$ ) are also indicated, together with the direction of magnetic field parallel ( $B_{||}$ ) and transverse ( $B_{\perp}$ ) to the JJ, and the magnetic flux  $\Phi$  (generated by the out-of-plane field  $B_{\perp}$ ). **c**, False-colour scanning electron micrograph of the top part of a typical device, as in the dashed box shown in **b**. The colours are the same as those used in **b**.

coherence length and  $v_F$  is the Fermi velocity in the semiconductor), while the non-complete closure of the gap at  $\Phi = (2n + 1)\Phi_0/2$  is associated with the finite length  $L_1$  of the junction and with possible unintended asymmetries in the etched superconducting leads (see Methods and Extended Data Fig. 2 for further details). The finite sub-gap conductance at  $B_{||} = 0$  (see Fig. 2f) is due to a relatively high tunnelling transmission and can be suppressed by tuning  $V_{qpc}$  to be more negative, as shown in Extended Data Figs. 4 and 5.

As  $B_{||}$  is increased, discrete Andreev bound states (ABSs) enter the gap and move towards zero energy, as shown by flux-dependent separated conductance peaks at  $|V_{sd}| \approx 0.05\text{--}0.1$  mV in Fig. 2b for  $B_{||} = 250$  mT. We note that these states have an asymmetric flux dependence. We attribute this behaviour to the presence of a strong spin-orbit interaction and a finite Zeeman field, similar to what has been predicted and observed for quasi-one-dimensional systems<sup>25,26</sup>.

At higher values of  $B_{||}$ , a ZBP in conductance appears at  $\Phi = (2n + 1)\Phi_0/2$  (corresponding to  $\varphi \approx \pi$ ), whereas it vanishes when  $\Phi$  is set to  $2n\Phi_0$ , that is, when  $\varphi = 0$ , as shown in Fig. 2c for  $B_{||} = 525$  mT. The phase dependence of the ZBP is highlighted in Fig. 2g, which displays the conductance line-cuts for  $\varphi = 0, \pi$ .

At even higher fields, from 600 mT to 1 T, the ZBP extends over the whole  $\varphi$  range, except at  $\varphi \approx \pi$  where a relative minimum is observed (Fig. 2d, e, h). In this range of  $B_{||}$ , the state remains at zero energy for  $\varphi = 0$ , as shown in Fig. 2h, whereas it oscillates and moves to higher energies for  $\varphi \approx \pi$  (see Extended Data Fig. 4f). Above  $B_{||} = 1$  T, the induced gap softens, and the phase dependence of sub-gap states gradually disappears as the JJs of the SQUID reach the resistive state.

The observed behaviour of the ZBP in field and phase is in good qualitative agreement with the calculated spectrum of a finite-size topological JJ, as shown in Extended Data Fig. 2. As the Zeeman field

is increased, two discrete sub-gap states are expected to merge at zero energy for  $\varphi = \pi$  and gradually extend in phase until reaching  $\varphi = 0$ . The calculated gapped zero-energy state around  $\varphi = 0$  is characterized by a Majorana wavefunction localized at the edges of the JJ (see Extended Data Fig. 2h). The oscillations in energy of the observed state at  $\varphi \approx \pi$  are reproduced by the simulations and can be understood in terms of hybridization of the Majorana modes (Extended Data Fig. 2i), because at this value of  $\varphi$  the induced gap is minimized and, as a result, the coherence length is maximized.

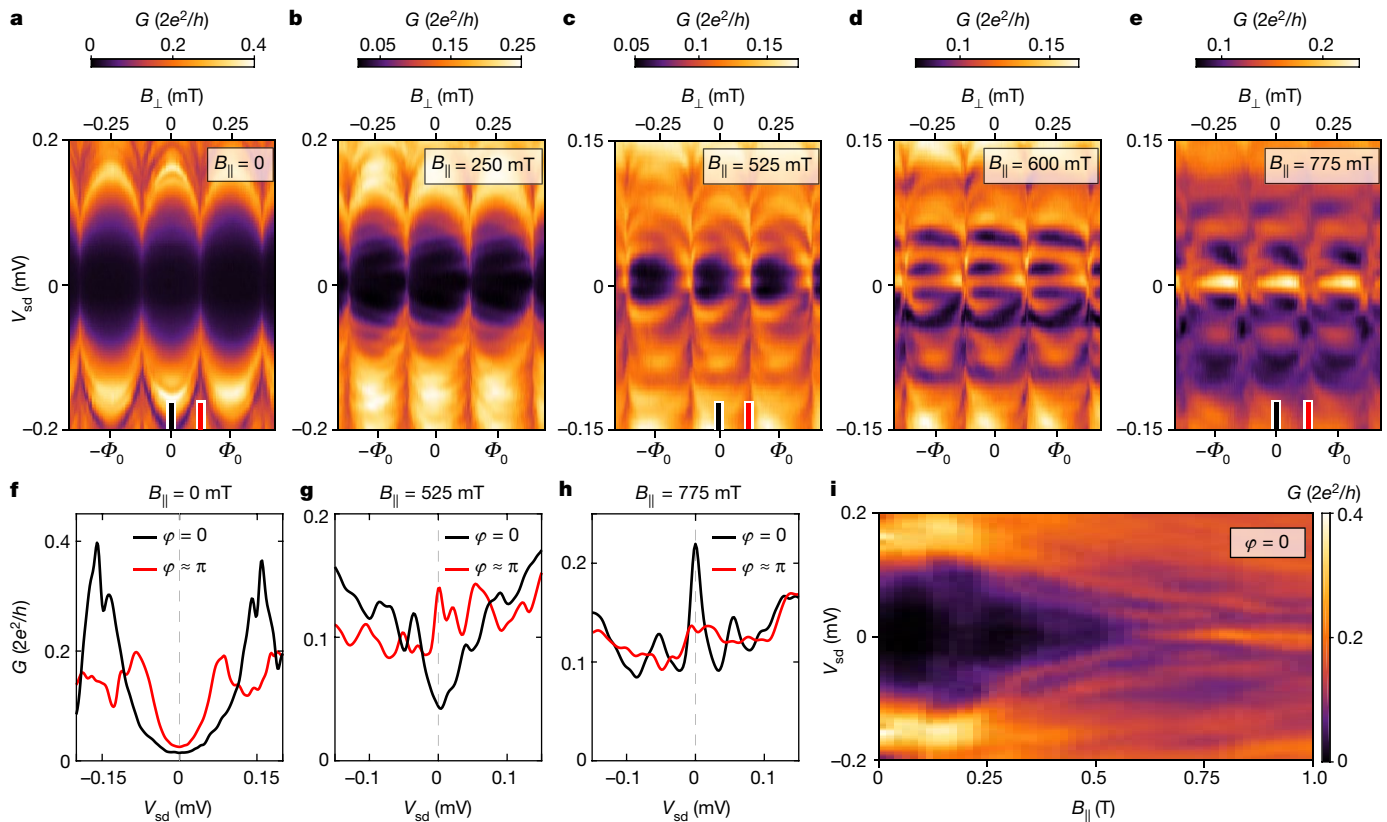
One of the most interesting features predicted for a perfectly transparent JJ is the expansion of the topological phase in magnetic field and chemical potential at  $\varphi = \pi$  (ref. 10). We therefore investigated the stability of the ZBP, starting from its dependence on the gate voltage  $V_1$ , which controls the chemical potential in JJ1. To efficiently explore our 4D parameter space, we recorded the third harmonic  $I_{3\omega}(V_{sd})$  of the current measured by the lock-in amplifier (this gives information about the conductance curvature at zero bias without the need for sweeping  $V_{sd}$ , reducing the 4D parameter space by one dimension). As shown in the Methods and in Extended Data Fig. 6,  $I_{3\omega}(V_{sd}) \propto -G''(V_{sd}) = -(\partial^2 G / \partial V^2)|_{V_{sd}}$ . A ZBP in conductance is therefore identified by a positive value of  $I_{3\omega}(V_{sd} = 0)$ , that is, by a negative value of  $G''(V_{sd} = 0)$ , which indicates a negative curvature around  $V_{sd} = 0$ .

Figure 3 displays  $I_{3\omega}(V_{sd} = 0)$  as a function of  $\Phi$  and  $V_1$  for different values of  $B_{||}$ . At  $B_{||} = 500$  mT, horizontal stripes showing positive values of  $I_{3\omega}(V_{sd} = 0)$  are visible at  $\varphi \approx (2n + 1)\pi$ . Increasing the field causes the region of negative curvature to expand around the voltage  $V_1^* = -118.5$  mV by around 2 mV and in phase extending to  $2n\pi$ . For  $B_{||} = 650$  mT, the ZBP region expands further around  $V_1^*$ , while a maximum develops at  $\varphi \approx (2n + 1)\pi$ , indicating that the ZBP has split to finite energy. The ZBP region covers a maximum range of 10 mV at 775 mT and remains extended in phase for  $\varphi \neq (2n + 1)\pi$ .

The finite range of  $V_1$  over which the ZBP is stable is explained by the narrow width  $W_{S1} \ll \xi_s$  of the superconducting leads, which effectively decrease the ratio between Andreev and normal reflection probabilities, thus reducing the size of the topological phase as a function of  $\mu$  (see Extended Data Figs. 1a and 2a). Although this geometry causes a deviation from the predicted behaviour of a topological JJ, in our devices the finite width is necessary to guarantee a well-defined induced gap up to 1 T (see Methods for further details).

The complementary study of the ZBP stability in  $\Phi$  and  $B_{||}$  for different values of  $V_1$  is shown in Fig. 4. At  $V_1 = -116$  mV (Fig. 4a), extended regions of positive  $I_{3\omega}(V_{sd} = 0)$  indicating a stable ZBP appear above an oscillating critical field  $B_c(\varphi)$ , which reaches a minimum value of  $B_c([2n + 1]\pi) = 570$  mT, as indicated by the blue arrow. On the other hand, the vertical stripe visible at  $B_{||} \approx 0.4$  T is due to ABSs crossing zero energy without sticking. Similar to what was observed above as a function of the chemical potential, the negative curvature region expands in terms of  $B_{||}$  range for  $V_1 = V_1^*$ , where  $B_c([2n + 1]\pi) = 435$  mT (Fig. 4b). At more negative  $V_1$ , the ZBP regime contracts again ( $B_c([2n + 1]\pi) = 480$  mT, Fig. 4c), consistent with the stability maps shown in Fig. 3.

The combined results shown in Figs. 3 and 4 indicate the expansion of the ZBP region from  $\varphi \approx \pi$  to the full phase range as  $B_{||}$  is increased. This behaviour is in qualitative agreement with the topological phase diagrams calculated for our system (see Extended Data Figs. 1a, b and 2a, b). We note that for specific values of chemical potential, the model of a perfectly symmetric and clean JJ predicts a topological phase transition close to zero field (see Extended Data Fig. 1), while experimentally a ZBP is observed only above 400 mT, as discussed above. This discrepancy could be ascribed to non-idealities of JJ1, such as disorder<sup>27,28</sup> and unintended asymmetries in the superconducting leads (see Extended Data Fig. 2). A broken left-right symmetry in JJ1 could also explain the observed asymmetry in the phase dependence of the ZBP region at different values of  $V_1$  (Fig. 4). Although we do not observe a reduction of the critical field down to zero, our design decreases  $B_c$  by about a



**Fig. 2 | Evolution of the zero-bias peak in parallel field.** **a–e**, Differential conductance  $G$  as a function of magnetic flux  $\Phi$  threading the SQUID loop and source–drain bias  $V_{sd}$  measured at different values of magnetic field  $B_{||}$  parallel to the junction. The flux is generated by the out-of-plane field  $B_{\perp}$ . The values of  $B_{\perp}$  have been shifted to remove offsets. **f–h**, Line-cuts of  $G$

versus  $V_{sd}$  at different values of  $B_{||}$  for phase bias  $\varphi = 0$  (black lines) and  $\varphi \approx \pi$  (red lines), as indicated by the black and red ticks in **a**, **c** and **e**. **i**,  $G$  as a function of  $V_{sd}$  and  $B_{||}$  at  $\varphi = 0$ . The plot was reconstructed from line-cuts like those shown in **f** and **g**. The measurements were taken at top gate voltage  $V_1 = V_1^* = -118.5$  mV.

factor of 4 compared with previous experiments on 1D Majorana wires defined below Al stripes in similar heterostructures<sup>6,7</sup>. This is due to the increased  $g$ -factor of the bare InAs Majorana channel and to the phase dependence of the observed ZBP. As expected, the amplitude of the  $B_c$  modulations depends on the value of  $V_1$  and a maximum visibility  $\{B_c(2n\pi) - B_c([2n+1]\pi)\}/B_c([2n+1]\pi) \approx 37\%$  is obtained for  $V_1 = V_1^*$ . Lastly, we note that the ZBP is robust over a range of  $\sim 70$  mV in  $V_{qpc}$  and in  $V_{top}$ , which modify the above-gap conductance by approximately an order of magnitude, as shown in Extended Data Fig. 4c,d.

As another test of the topological nature of the observed ZBPs, we performed spectroscopy as a function of the magnetic field  $B_t$  applied in the plane of the 2DEG but orthogonal to the 1D channel defined by

JJ1 (see Fig. 1b). In this field orientation, we do not observe any discrete state sticking at zero energy before the suppression of the induced gap, which occurs at  $B_t \approx 360$  mT (see Extended Data Fig. 3).

Finally, it is worth noting that a first-order topological transition is expected for a planar JJ in presence of strong parallel fields. This transition should manifest itself with a minimum of the Josephson critical current<sup>29</sup> when the Zeeman energy reaches a value comparable to the Thouless energy  $E_T$  (ref. <sup>10</sup>). In our case, however, this limit cannot be reached because  $E_T \approx 2.8$  meV is an order of magnitude larger than  $\Delta$ . Experimentally, we observed periodic revivals of the Josephson current flowing through JJ1 as a function of  $B_{||}$ , with a periodicity correlated to  $W_{S1}$  (see Extended Data Fig. 10). We ascribe

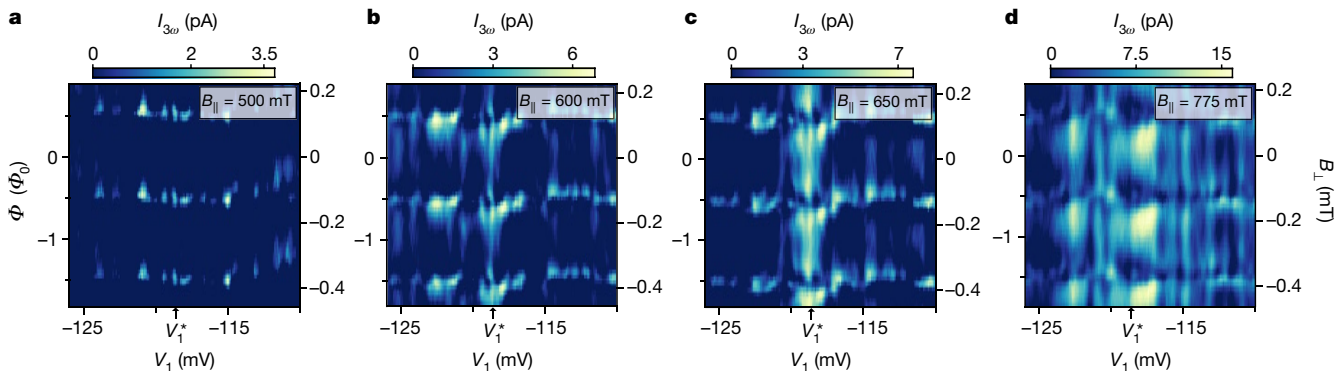


**Fig. 3 | Stability of the zero-bias peak.** **a–d**, Third harmonic of the current  $I_{3\omega}(V_{sd}=0)$  measured by the lock-in amplifier at zero bias as a function of gate voltage  $V_1$  and  $\Phi$ , for different values of  $B_{||}$ . The flux is generated by  $B_{\perp}$ . The values of  $B_{\perp}$  have been shifted to remove offsets.

As shown in the Methods and in Extended Data Fig. 6,  $I_{3\omega}(V_{sd}=0) \propto -G''(V_{sd}=0)$ , where  $G''(V_{sd}=0) = (\partial^2 G / \partial V^2)|_{V_{sd}=0}$  is the second derivative of the conductance at zero bias. A positive value of  $I_{3\omega}(V_{sd}=0)$  corresponds to a ZBP in conductance as a function of  $V_{sd}$ .

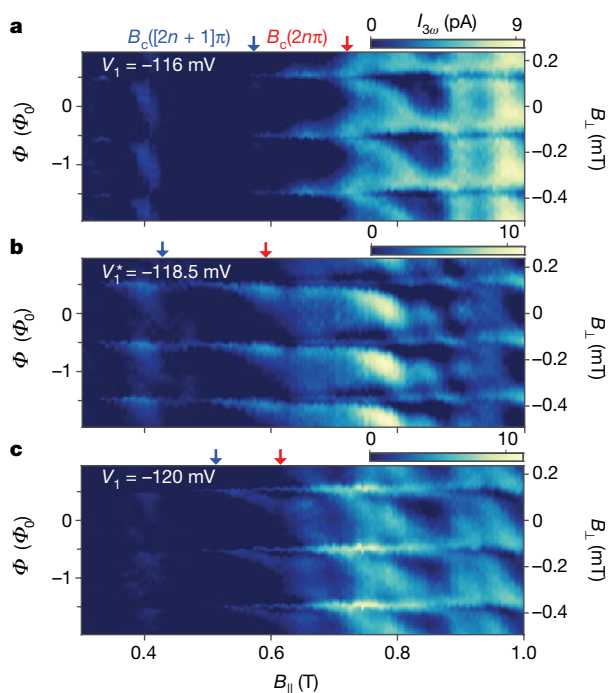


**Fig. 4 | Phase dependence of the critical field.** a–c, Third harmonic of the current  $I_{3\omega}$  ( $V_{sd} = 0$ ) measured by the lock-in amplifier at zero bias as a function of  $B_{||}$  and  $\Phi$ , for different values of gate voltage  $V_1$ . The flux is generated by  $B_{\perp}$ . The values of  $B_{\perp}$  have been shifted to remove offsets. A positive value of  $I_{3\omega}$  ( $V_{sd} = 0$ ) corresponds to a ZBP in conductance as a function of  $V_{sd}$ .

this behaviour to trivial orbital effects of the in-plane magnetic field in the proximitized 2DEG underneath the superconducting leads<sup>10</sup>.

In summary, we have investigated phase-dependent ZBPs in tunnelling conductance measured at the edge of a JJ patterned in a 2D InAs/Al heterostructure. The critical field at which the ZBP appears depends on the phase bias and is minimal at  $\varphi \approx \pi$ , as expected for a topological JJ. We studied the ZBP stability as a function of field  $B_{||}$ , phase  $\varphi$  and chemical potential  $\mu$ , obtaining results qualitatively consistent with the topological phase diagram of a finite-size junction. Future material<sup>30–32</sup> and design improvements might allow the investigation of JJs with  $W_{S1} \gg \xi_S$ , where the influence of  $\mu$  is expected to be suppressed<sup>10</sup>. Together with our top-down fabrication approach, the phase tuning of topological channels without the need for careful gate tuning would greatly simplify the realization of sophisticated network geometries required to implement topologically protected quantum devices<sup>9,12,13</sup>.

## Online content

Any methods, additional references, Nature Research reporting summaries, source data, statements of data availability and associated accession codes are available at <https://doi.org/10.1038/s41586-019-1068-8>.

Received: 6 September 2018; Accepted: 24 January 2019;

Published online 24 April 2019.

1. Kitaev, A. Fault-tolerant quantum computation by anyons. *Ann. Phys.* **303**, 2–30 (2003).
2. Nayak, C., Simon, S. H., Stern, A., Freedman, M. & Das Sarma, S. Non-Abelian anyons and topological quantum computation. *Rev. Mod. Phys.* **80**, 1083–1159 (2008).
3. Mourik, V. et al. Signatures of Majorana fermions in hybrid superconductor–semiconductor nanowire devices. *Science* **336**, 1003–1007 (2012).
4. Das, A. et al. Zero-bias peaks and splitting in an Al–InAs nanowire topological superconductor as a signature of Majorana fermions. *Nat. Phys.* **8**, 887–895 (2012).
5. Deng, M. T. et al. Majorana bound state in a coupled quantum-dot hybrid-nanowire system. *Science* **354**, 1557–1562 (2016).
6. Suominen, H. J. et al. Zero-energy modes from coalescing Andreev states in a two-dimensional semiconductor–superconductor hybrid platform. *Phys. Rev. Lett.* **119**, 176805 (2017).
7. Nichele, F. et al. Scaling of Majorana zero-bias conductance peaks. *Phys. Rev. Lett.* **119**, 136803 (2017).
8. Zhang, H. et al. Quantized Majorana conductance. *Nature* **556**, 74–79 (2018).

9. Hell, M., Leijnse, M. & Flensberg, K. Two-dimensional platform for networks of Majorana bound states. *Phys. Rev. Lett.* **118**, 107701 (2017).
10. Pientka, F. et al. Topological superconductivity in a planar Josephson junction. *Phys. Rev. X* **7**, 021032 (2017).
11. Casparis, L. et al. Superconducting gatemon qubit based on a proximitized two-dimensional electron gas. *Nat. Nanotechnol.* **13**, 915–919 (2018).
12. Hell, M., Flensberg, K. & Leijnse, M. Coupling and braiding Majorana bound states in networks defined in two-dimensional electron gases with proximity-induced superconductivity. *Phys. Rev. B* **96**, 035444 (2017).
13. Stern, A. & Berg, E. Fractional Josephson vortices and braiding of Majorana zero modes in planar superconductor–semiconductor heterostructures. *Phys. Rev. Lett.* **122**, 107701 (2019).
14. Shabani, J. et al. Two-dimensional epitaxial superconductor–semiconductor heterostructures: a platform for topological superconducting networks. *Phys. Rev. B* **93**, 155402 (2016).
15. Krogstrup, P. et al. Epitaxy of semiconductor–superconductor nanowires. *Nat. Mater.* **14**, 400–406 (2015).
16. Kjaergaard, M. et al. Quantized conductance doubling and hard gap in a two-dimensional semiconductor–superconductor heterostructure. *Nat. Commun.* **7**, 12841 (2016).
17. Kjaergaard, M. et al. Transparent semiconductor–superconductor interface and induced gap in an epitaxial heterostructure Josephson junction. *Phys. Rev. Appl.* **7**, 034029 (2017).
18. Blonder, G. E., Tinkham, M. & Klapwijk, T. M. Transition from metallic to tunneling regimes in superconducting micro-constrictions: excess current, charge imbalance, and supercurrent conversion. *Phys. Rev. B* **25**, 4515–4532 (1982).
19. Klapwijk, T. M. Proximity effect from an Andreev perspective. *J. Supercond.* **17**, 593–611 (2004).
20. Lutchyn, R. M., Sau, J. D. & Das Sarma, S. Majorana fermions and a topological phase transition in semiconductor–superconductor heterostructures. *Phys. Rev. Lett.* **105**, 077001 (2010).
21. Oreg, Y., Refael, G. & von Oppen, F. Helical liquids and Majorana bound states in quantum wires. *Phys. Rev. Lett.* **105**, 177002 (2010).
22. Tinkham, M. *Introduction to Superconductivity* (Dover, Mineola, 2004).
23. Andreev, A. F. The thermal conductivity of the intermediate state in superconductors. *Sov. Phys. JETP* **19**, 1228–1231 (1964).
24. Kulik, I. O. Macroscopic quantization and the proximity effect in S–N–S junctions. *Sov. Phys. JETP* **30**, 944–950 (1970).
25. Yokoyama, T., Eto, M. & Nazarov, V. Y. Josephson current through semiconductor nanowire with spin–orbit interaction in magnetic field. *J. Phys. Soc. Jpn* **82**, 054703 (2013).
26. van Woerkom, D. J. et al. Microwave spectroscopy of spinful Andreev bound states in ballistic semiconductor. *Nat. Phys.* **13**, 876–881 (2017).
27. Haim, A. & Stern, A. The double-edge sword of disorder in multichannel topological superconductors. <https://arxiv.org/abs/1808.07886> (2018).
28. Suominen, H. J. et al. Anomalous Fraunhofer interference in epitaxial superconductor–semiconductor Josephson junctions. *Phys. Rev. B* **95**, 035307 (2017).
29. Hart, S. et al. Controlled finite momentum pairing and spatially varying order parameter in proximitized HgTe quantum wells. *Nat. Phys.* **13**, 87–93 (2016).
30. Drachmann, A. C. C. et al. Proximity effect transfer from NbTi into a semiconductor heterostructure via epitaxial aluminum. *Nano Lett.* **17**, 1200–1203 (2017).
31. Delfanazari, K. et al. On-chip Andreev devices: hard superconducting gap and quantum transport in ballistic Nb–In<sub>0.75</sub>Ga<sub>0.25</sub>As–quantum-well–Nb Josephson junctions. *Adv. Mater.* **29**, 1701836 (2017).
32. Thomas, C. et al. High-mobility InAs 2DEGs on GaSb substrates: a platform for mesoscopic quantum transport. *Phys. Rev. Mater.* **2**, 104602 (2018).

**Acknowledgements** This work was supported by Microsoft Corporation, the Danish National Research Foundation, the Villum Foundation, ERC Project MUNATOP, CRC-183 and the Israeli Science Foundation. We thank E. O’Farrell, M. Hell, K. Flensberg and J. Folk for discussions.

**Reviewer information** Nature thanks Kaveh Delfanazari and the other anonymous reviewer(s) for their contribution to the peer review of this work.

**Author contributions** S.G., C.T., T.W., R.K., G.C.G. and M.J.M. developed and grew the InAs/Al heterostructure. A.F., A.M.W. and A.C.C.D. fabricated the devices. A.F., A.M.W. and A.C.C.D. performed the measurements with input from C.M.M. and F.N. Data analysis was done by A.F., A.M.W. and E.P.M. F.S., A.K., E.B. and A.S. developed the theoretical model and carried out the simulations. C.M.M. and F.N. conceived the experiment. All authors contributed to interpreting the data. The manuscript was written by A.F., A.M.W., C.M.M. and F.N. with suggestions from all other authors.

**Competing interests** The authors declare no competing interests.

## Additional information

**Extended data** is available for this paper at <https://doi.org/10.1038/s41586-019-1068-8>.

**Reprints and permissions information** is available at <http://www.nature.com/reprints>.

**Correspondence and requests for materials** should be addressed to C.M.M. or F.N.

**Publisher’s note:** Springer Nature remains neutral with regard to jurisdictional claims in published maps and institutional affiliations.

© The Author(s), under exclusive licence to Springer Nature Limited 2019

## METHODS

**Wafer structure.** The wafer structure used for this work was grown on an insulating InP substrate by molecular beam epitaxy. From bottom to top, it comprises a 100-nm-thick  $\text{In}_{0.52}\text{Al}_{0.48}\text{As}$  matched buffer, a 1- $\mu\text{m}$ -thick step-graded buffer realized with alloy steps from  $\text{In}_{0.52}\text{Al}_{0.48}\text{As}$  to  $\text{In}_{0.89}\text{Al}_{0.11}\text{As}$  (20 steps, 50 nm per step), a 58-nm  $\text{In}_{0.82}\text{Al}_{0.18}\text{As}$  layer, a 4-nm  $\text{In}_{0.75}\text{Ga}_{0.25}\text{As}$  bottom barrier, a 7-nm InAs quantum well, a 10-nm  $\text{In}_{0.75}\text{Ga}_{0.25}\text{As}$  top barrier, two monolayers of GaAs and a 7-nm film of epitaxial Al. The top Al layer was grown in the same molecular beam epitaxy chamber used for the rest of the growth, without breaking the vacuum. This results in semiconductor–superconductor interfaces characterized by almost unitary transparency<sup>17</sup>. The two monolayers of GaAs are introduced to help to passivate the wafer surface where the Al film is removed, and to make the sample more compatible with our Al etchant. The 2DEG is expected to reside mainly in the InAs quantum well, with the upper tail of the wavefunction extending to the Al film<sup>14</sup>.

Characterization performed in a Hall bar geometry where the Al was removed revealed an electron mobility peak of  $43,000 \text{ cm}^2 \text{ V}^{-1} \text{ s}^{-1}$  for an electron density  $n = 8 \times 10^{11} \text{ cm}^{-2}$ , corresponding to an electron mean free path of  $l_e \approx 600 \text{ nm}$ . Electron transport through JJ1 is therefore expected to be ballistic along the width direction ( $l_e \gg L_1$ ) and diffusive along the length direction ( $L_1 > l_e$ ). Characterization of a large-area Al film revealed a critical magnetic field of 2.5 T when the field was applied in the plane of the 2DEG.

**Device fabrication.** Samples were fabricated with conventional electron beam lithography techniques. First, we isolated large mesa structures by locally removing the top Al layer (with Al etchant Transene D) and performing a deep III–V chemical wet etch (220:55:33  $\text{H}_2\text{O}:\text{C}_6\text{H}_8\text{O}_7:\text{H}_3\text{PO}_4:\text{H}_2\text{O}_2$ ). In a subsequent step, we patterned the Al SQUID by selectively removing the top Al layer with a wet etch (Transene D) at a temperature of  $(50 \pm 1)^\circ\text{C}$  for 5 s. We then deposited on the entire sample a 15-nm-thick layer of insulating  $\text{HfO}_2$  by atomic layer deposition at a temperature of  $90^\circ\text{C}$ . The top gate electrodes were deposited in two successive steps. First, we defined the features requiring high accuracy and deposited 5 nm of Ti and 25 nm of Au by electron beam evaporation. In a successive step, we defined the gate bonding pads by evaporating 10 nm of Ti and 350 nm of Au. Ohmic contacts to the InAs were provided by the epitaxial Al layer, which is contacted directly by wedge bonding through the insulating  $\text{HfO}_2$ .

**Measurements.** Electrical measurements were performed in a dilution refrigerator with a base temperature of 15 mK with conventional DC and lock-in techniques using low frequencies ( $\nu < 200 \text{ Hz}$ ) excitations. To measure the differential conductance  $G = dI/dV$ , an a.c. voltage bias of  $V_{ac} = 3 \mu\text{V}$ , superimposed on a variable d.c. bias  $V_{sd}$ , was applied to the top lead of the device (see Fig. 1b), with one of the SQUID leads grounded via a low-impedance current-to-voltage converter. An a.c. voltage amplifier with an input impedance of 500 M $\Omega$  was used to measure the four-terminal voltage across the device. Information about the second derivative of the conductance  $G''(V_{sd}) = (\partial^2 G / \partial V^2)|_{V_{sd}}$  was experimentally obtained by recording the third harmonic  $I_{3\omega}(V_{sd})$  of the current measured by the lock-in amplifier (model SR830, which enables the detection of signals at harmonics of the reference frequency). Indeed, when a sinusoidal time-dependent excitation  $V(t) = V_{sd} + V_{ac}\sin(\omega t)$  is applied to the device, the measured output current can be expanded in Taylor's series as:

$$I(t) \simeq I(V_{sd}) + \frac{\partial I}{\partial V} \bigg|_{V_{sd}} V_{ac}\sin(\omega t) + \frac{1}{2} \frac{\partial^2 I}{\partial V^2} \bigg|_{V_{sd}} [V_{ac}\sin(\omega t)]^2 + \frac{1}{6} \frac{\partial^3 I}{\partial V^3} \bigg|_{V_{sd}} [V_{ac}\sin(\omega t)]^3. \quad (1)$$

Since  $[\sin(\omega t)]^3 = 1/4[-\sin(3\omega t) + 3\sin(\omega t)]$ , we obtain:

$$I_{3\omega}(V_{sd}) = -\frac{1}{24} \frac{\partial^3 I}{\partial V^3} \bigg|_{V_{sd}} V_{ac}^3 \propto -\frac{\partial^2 G}{\partial V^2} \bigg|_{V_{sd}}. \quad (2)$$

To increase the signal-to-noise ratio, the measurement of  $I_{3\omega}(V_{sd})$  was performed with an amplitude  $V_{ac}$  of the excitation greater than the temperature-limited full-width at half-maximum of a Lorentzian feature, that is,  $V_{ac} \approx 3.5 k_B T$ , where  $k_B$  is the Boltzmann constant and  $T \approx 40 \text{ mK}$  is the electron temperature in our devices. The comparison between  $I_{3\omega}(V_{sd})$  and  $G''(V_{sd})$  is shown in Extended Data Fig. 6.

The SQUID device was separately characterized. The SQUID differential resistance  $R = dV/dI$  was obtained by applying an a.c. bias  $I_{ac} < 5 \text{ nA}$ , superimposed on a variable d.c. bias  $I_{dc}$ , to the superconducting leads of the interferometer, with the tunnelling probe closed and floating. The behaviour of the Josephson critical current is shown in Extended Data Figs. 9 and 10.

We studied seven devices characterized by different dimensions of JJ1. Devices 1 and 2 (nominally identical) have  $W_1 = 80 \text{ nm}$  and  $W_{S1} = 160 \text{ nm}$ , device 3 has

$W_1 = 120 \text{ nm}$  and  $W_{S1} = 160 \text{ nm}$ , device 4 has  $W_1 = 40 \text{ nm}$  and  $W_{S1} = 160 \text{ nm}$ , device 5 has  $W_1 = 160 \text{ nm}$  and  $W_{S1} = 160 \text{ nm}$ , device 6 has  $W_1 = 80 \text{ nm}$  and  $W_{S1} = 500 \text{ nm}$ , and device 7 has  $W_1 = 80 \text{ nm}$  and  $W_{S1} = 1 \mu\text{m}$ . All the devices were designed with  $L_1 = 1.6 \mu\text{m}$ ,  $W_2 = 40 \text{ nm}$ ,  $L_2 = 5 \mu\text{m}$  and  $W_{S2} = 160 \text{ nm}$ . In device 3, spectroscopy was performed by means of a QPC coupling JJ1 to a wide Al plane, following the approach of refs<sup>6,7</sup> (see Extended Data Fig. 8 for further details). Results consistent with those presented in the main text were obtained in devices 1, 2 and 3, whereas devices 4 and 5 did not show robust ZBPs in field. In devices 6 and 7, the induced superconducting gap collapsed at  $B_{||} \approx 200 \text{ mT}$  without showing any robust ZBP. The behaviour of devices 6 and 7 is consistent with the softening of the induced gap in low parallel fields observed below wide superconducting leads<sup>6,16</sup>.

**Theoretical model.** We model JJ1 of the measured device using the Hamiltonian<sup>9,10</sup> written in the Nambu basis  $(\psi_p, \psi_l, \psi_l^\dagger, -\psi_p^\dagger)^T$  as

$$H = \left( -\frac{\hbar^2 (\partial_x^2 + \partial_y^2)}{2m^*} - \mu \right) \tau_z + \alpha (i\partial_y \sigma_x - i\partial_x \sigma_y) \tau_z + E_Z \sigma_y + \Delta(x) \tau_+ + \Delta^*(x) \tau_-, \quad (3)$$

where  $\psi_{l,\downarrow}$  are the annihilation operators for electrons with spin up and down,  $\sigma$  and  $\tau$  are the Pauli matrices acting in the spin and particle–hole basis, respectively, with  $\tau_\pm = (\tau_x \pm i\tau_y)/2$ . Here,  $m^*$  is the effective electron mass,  $\mu$  is the chemical potential,  $\alpha$  is the spin–orbit coupling strength of InAs,  $E_Z = g\mu_B B_{||}/2$  is the Zeeman field strength due to the applied magnetic field along the junction ( $y$  direction) and  $\Delta(x)$  is the proximity-induced pairing potential. The proximity-induced pairing potential is taken to be non-zero in the 2DEG below the superconducting leads and zero in the junction, that is,

$$\Delta(x) = \begin{cases} \Delta_L e^{-i\varphi/2} & \text{for } -(W_l/2 + W_{S1}) < x < -W_l/2, \\ 0 & \text{for } -W_l/2 < x < W_l/2, \\ \Delta_R e^{i\varphi/2} & \text{for } W_l/2 < x < W_l/2 + W_{S1}, \end{cases} \quad (4)$$

where  $\Delta_L$  ( $\Delta_R$ ) is the left (right) proximity-induced pairing potential,  $\varphi$  is the superconducting phase difference between the two superconductors, and  $W_l$  and  $W_{S1}$  are the widths of the junction and superconducting leads, respectively. The Zeeman field  $E_Z$  is taken to be uniform throughout the system. Numerical simulations in this paper are done using experimental parameters:  $m^* = 0.026m_e$  (ref. <sup>33</sup>),  $\alpha = 0.1 \text{ eV \AA}$  (ref. <sup>34</sup>),  $W_l = 80 \text{ nm}$  and  $W_{S1} = 160 \text{ nm}$ . We consider two cases: (1) left–right symmetric junctions ( $\Delta_L = \Delta_R = 0.15 \text{ meV}$ ) and (2) left–right asymmetric junctions ( $\Delta_L = 0.15 \text{ meV}$  and  $\Delta_R = 0.1 \text{ meV}$ ). The first case corresponds to an idealized clean system, whereas the second case takes into account the combined effects of disorder<sup>27,28</sup>, variations in the geometrical widths of the etched superconducting leads and different couplings between the superconductor and the semiconductor.

**Phase diagram.** We study the phase diagram of the system as a function of the in-plane Zeeman field, phase difference across the junction, and chemical potential. In the limit of very wide superconducting leads ( $W_{S1} \gg \xi_S$  where  $\xi_S = \hbar v_F / \pi \Delta$  is the superconducting coherence length and  $v_F$  is the Fermi velocity in the semiconductor), the topological phase transition depends on both the phase bias across the junction and the in-plane Zeeman field, with very weak dependence on the chemical potential<sup>9,10</sup>. However, when the superconducting leads are narrow ( $W_{S1} \ll \xi_S$ ), we expect the phase diagram to have a stronger dependence on the chemical potential and a weaker dependence on the phase bias, owing to strong normal reflections from the superconductor edges.

To obtain the phase diagram of the system, we perform numerical simulations of the tight-binding version of the Hamiltonian (equation (3)) obtained using the Kwant package<sup>35</sup>. We calculate the  $\mathbb{Z}_2$  topological invariant  $Q = \text{sign}[\text{Pf}(H_{k_y=\pi\sigma_y\tau_y}) / \text{Pf}(H_{k_y=0\sigma_y\tau_y})]^{36,37}$ , where  $Q = \pm 1$  and Pf is the Pfaffian operator, for an infinitely long junction. The calculated phase diagrams for a left–right symmetric junction are shown in Extended Data Fig. 1a, b. The topological phase transition boundary, which separates the trivial region ( $Q = 1$ ) at low Zeeman field from the topological region ( $Q = -1$ ) at high Zeeman field, is marked by a gap closing at  $k_y = 0$ . This topological transition corresponds to the transition between even (trivial) and odd (topological) number of subbands crossed by the Fermi level. For our case of narrow superconducting leads ( $W_{S1} \ll \xi_S$ ), the  $\mathbb{Z}_2$  topological phase diagrams are weakly dependent on the superconducting phase difference (see Extended Data Fig. 1a). Extended Data Fig. 1a also shows that for junctions with narrow superconducting leads, the dependence of the topological phase diagram on the superconducting phase difference is stronger for the case where the chemical potential is in the regime where the topological transition happens at a smaller Zeeman field. The phase diagram as a function of superconducting phase difference and chemical potential is shown in Extended Data Fig. 1b.

**Energy spectra and Majorana wave function.** We calculate the energy spectra and Majorana wave functions by diagonalizing the tight-binding Hamiltonian,

obtained using the Kwant package<sup>35</sup>, for a finite-length system ( $L_1 = 1.6 \mu\text{m}$ ). Extended Data Fig. 1c–g shows the energy spectrum of the system as a function of the superconducting phase difference for several values of Zeeman field strengths. The spectrum shows a modulation with respect to the superconducting phase difference where the bulk gap assumes its minimum value at  $\varphi = \pi$ . In the limit where the junction is infinitely long and there is an exact left–right symmetry between its two superconductors (including the geometric size and the magnitude of the superconducting order parameters), the gap closes at  $\varphi = \pi$ . This can be understood as follows. For narrow superconducting leads ( $W_{S1} \ll \xi_s$ ), which is the case that we discuss here, electrons have to undergo multiple normal reflections from the edges of the superconductors before they can be Andreev reflected, as it takes a length of about  $\xi_s$  for electrons to feel the presence of a gap. As a result, electrons feel a gap which is the weighted average of the left and right superconducting gaps, that is,

$$\begin{aligned}\tilde{\Delta} &= \frac{1}{2W_{S1} + W_1} \int_{-(W_1/2 + W_{S1})}^{W_1/2 + W_{S1}} \Delta(x) dx, \\ &= \Delta(e^{-i\varphi/2} + e^{i\varphi/2}) \frac{W_{S1}}{2W_{S1} + W_1}, \\ &= \Delta \frac{2W_{S1}}{2W_{S1} + W_1} \cos(\varphi/2),\end{aligned}\quad (5)$$

where the term  $2W_{S1}/(2W_{S1} + W_1)$  is the ratio of the width of the superconductors to the total width of the system. Furthermore, because the superconducting leads are narrow, the boundary of the topological region depends on the chemical potential. For specific values of the chemical potential, the boundary of the topological region at  $\varphi = \pi$  goes down all the way to zero Zeeman field, as shown in Extended Data Fig. 1a, c.

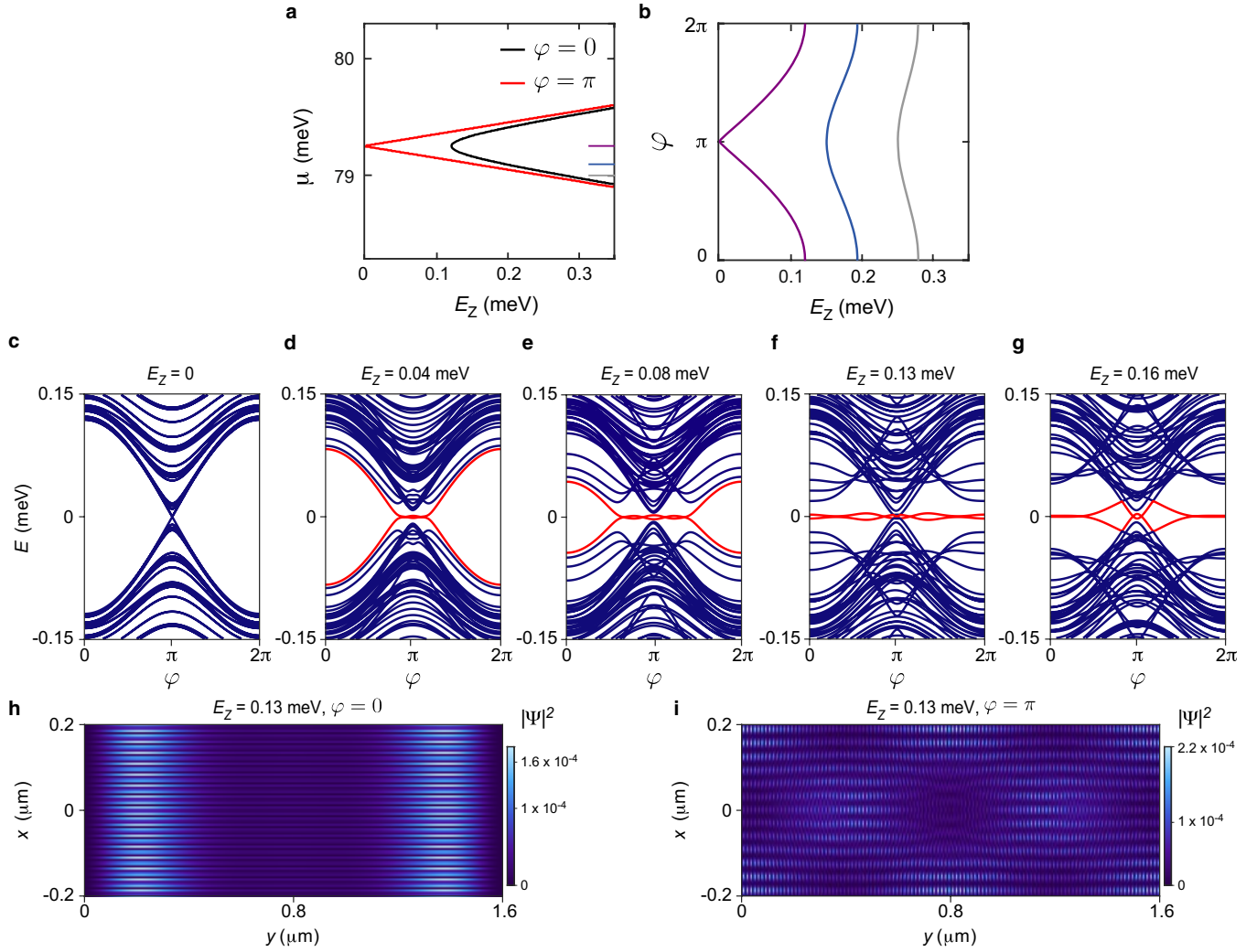
The left–right symmetry may be broken by disorder<sup>27,28</sup>, different geometric sizes of the superconducting leads or different coupling of the 2DEG to the superconductors on the two sides of the junctions. When it is broken, the gap does not necessarily close at  $\varphi = \pi$  and  $E_Z = 0$ . As a result, the topological phase boundary

line near  $\varphi = \pi$  shifts to higher Zeeman field strengths. We show this effect of left–right asymmetry in Extended Data Fig. 2a–c by introducing an asymmetry in the induced left- and right-induced superconducting pairing potentials ( $\Delta_L \neq \Delta_R$ ). For this case, the critical Zeeman field at  $\varphi = \pi$  shifts to  $E_Z \propto |\Delta_L - \Delta_R|$ . Yet, as long as the symmetry is not strongly broken, the smallest critical Zeeman field required for a topological phase is realized at  $\varphi = \pi$ . When the Zeeman field strength exceeds the critical value at which the topological phase transition happens, Majorana zero modes will appear at the end of the junction. The Majorana zero modes first appear at  $\varphi = \pi$  since for this value of  $\varphi$  the critical field is the lowest. As the Zeeman field strength is increased further, the range of phases where the Majorana modes occur increases. Extended Data Figs. 1h, i and 2h, i show the probability densities of the lowest energy wave functions (corresponding to Majorana modes) calculated using the experimental parameters of our system. As can be seen in the figure, for our system with a length of  $L_1 = 1.6 \mu\text{m}$ , in some parameter regimes the Majoranas are localized at the system end and are well separated from each other.

## Data availability

The data that support the findings of this study are available from the corresponding authors on reasonable request.

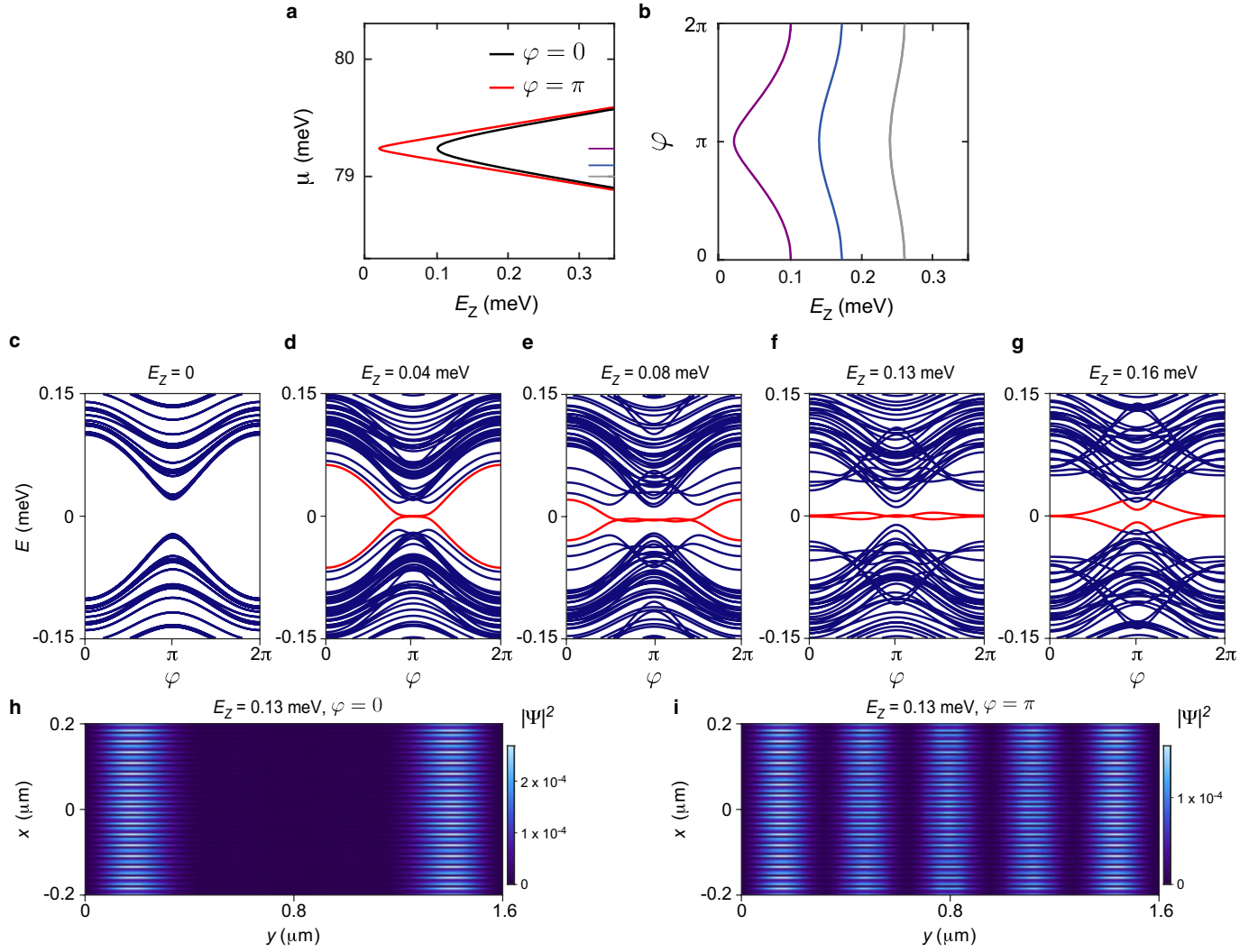
33. Vurgaftman, I., Meyer, J. R. & Ram-Mohan, L. R. Band parameters for III–V compound semiconductors and their alloys. *J. Appl. Phys.* **89**, 5815–5875 (2001).
34. O’Farrell, E. C. T. et al. Hybridization of sub-gap states in one-dimensional superconductor–semiconductor Coulomb islands. *Phys. Rev. Lett.* **121**, 256803 (2018).
35. Groth, C. W., Wimmer, M., Akhmerov, A. R. & Waintal, X. Kwant: a software package for quantum transport. *New J. Phys.* **16**, 063065 (2014).
36. Kitaev, A. Y. Unpaired Majorana fermions in quantum wires. *Phys. Uspekhi* **44**, 131 (2001).
37. Tewari, S. & Sau, J. D. Topological invariants for spin–orbit coupled superconductor nanowires. *Phys. Rev. Lett.* **109**, 150408 (2012).
38. Beenakker, C. W. J. Quantum transport in semiconductor–superconductor microjunctions. *Phys. Rev. B* **46**, 12841–12844 (1992).



### Extended Data Fig. 1 | Calculated spectra for a symmetric device.

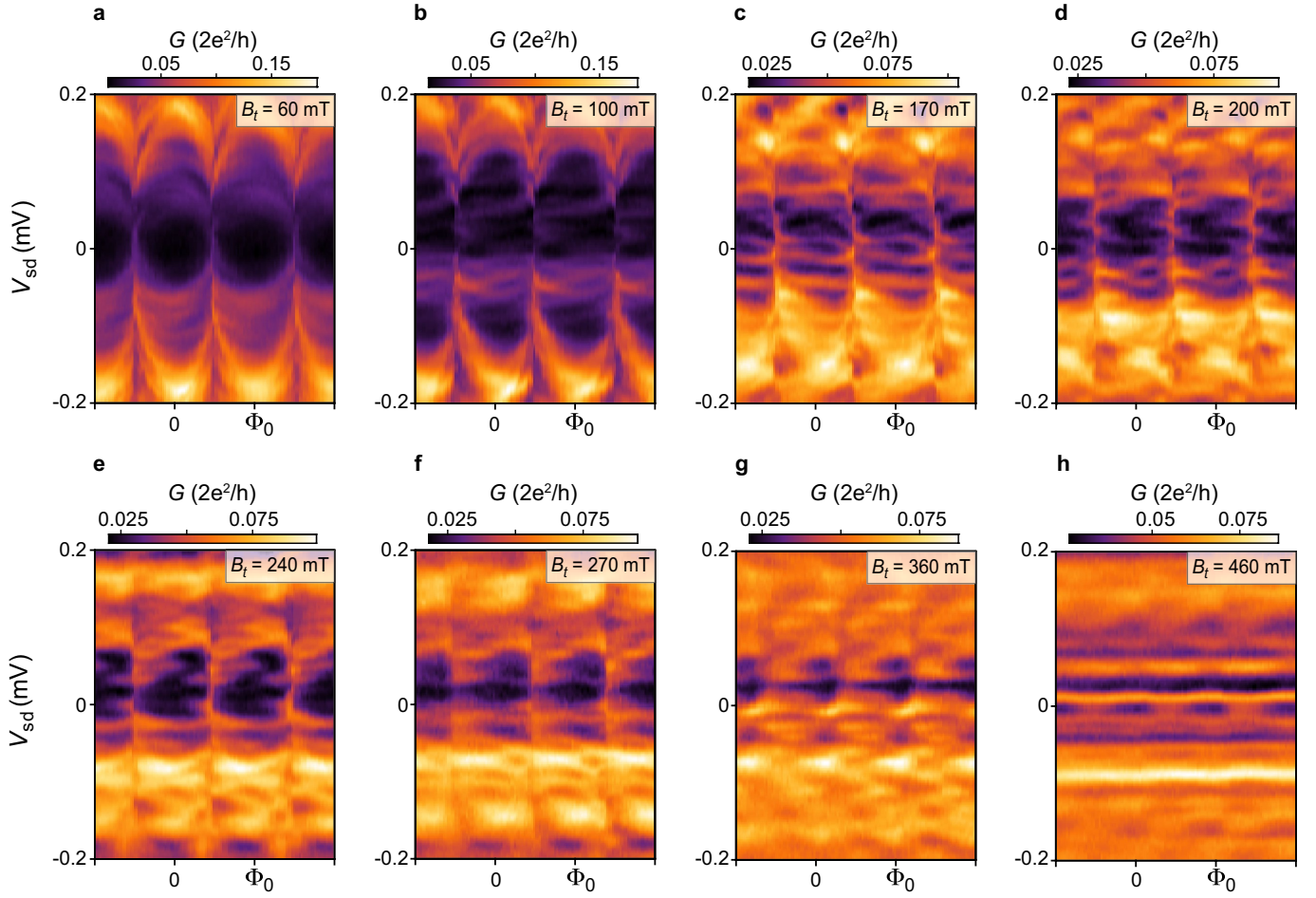
**a**, Topological phase diagram as a function of the Zeeman energy  $E_Z$  and the 2DEG chemical potential  $\mu$  for two values of the phase bias  $\varphi = 0, \pi$ , calculated from the tight-binding Hamiltonian for JJ1 with infinite length (see Methods) and symmetric superconducting leads. The curves indicate the critical value of  $E_Z$  above which the system is tuned into the topological phase. **b**, Topological phase diagram as a function of  $E_Z$  and  $\varphi$  for different values of  $\mu$ , as indicated by the horizontal ticks in **a**. The diagrams were calculated for a junction with width  $W_1 = 80$  nm, superconducting lead width  $W_{S1} = 160$  nm, induced gap  $\Delta_{L,R} = 150$   $\mu\text{eV}$  and Rashba spin-orbit coupling constant  $\alpha = 100$  meV  $\text{\AA}$ . The length of the junction  $L_1$  was assumed to be infinite in order to obtain a well-defined topological invariant, as described in the Methods. **c–g**, Calculated energy spectra as a function of  $\varphi$  for different values of the Zeeman energy. The spectra were obtained for the same parameters used in **a** and **b**, except for  $L_1 = 1.6$   $\mu\text{m}$ . For this left–right symmetric junction, the topological transition can occur at  $E_Z = 0$  for  $\varphi = \pi$  and specific values of chemical potential. We calculate the spectra and Majorana wavefunctions at this fine-tuned chemical potential  $\mu = 79.25$  meV (corresponding to the

purple curve in **b**). For the chosen parameters, the system undergoes a topological transition at  $E_Z = 0$  for  $\varphi = \pi$  and at  $E_Z = 0.12$  meV for  $\varphi = 0$ . The lowest-energy subgap states are shown in red and indicate two Majorana zero modes at the edges of the junction in the topological regime. As a function of  $E_Z$  these states first reach zero energy at  $\varphi = \pi$  and progressively extend in phase. At high values of  $E_Z$ , the Majorana modes oscillate around zero energy owing to their hybridization, caused by the finite size of our system. This is particularly evident at  $\varphi = \pi$ , where the induced gap is minimized and the coherence length is maximized. **h, i**, Probability density  $|\Psi|^2$  of the Majorana wavefunction calculated as a function of the spatial directions  $x$  and  $y$  in JJ1 for  $E_Z = 0.13$  meV and  $\varphi = 0, \pi$ . The  $x$  coordinate extends in the width direction including the superconducting leads ( $2W_{S1} + W_1$ ) =  $0.4$   $\mu\text{m}$ , with  $x = 0$  indicating the centre of the junction, while  $y$  is the coordinate along the length of the junction. The Majorana wavefunctions are localized in the  $y$  direction at the edges of the junction when the lowest energy states in the spectrum are close to zero energy. In the  $x$  direction, the Majorana modes are delocalized below the superconducting leads, owing to our geometry having  $W_{S1} \ll \xi_S$ .



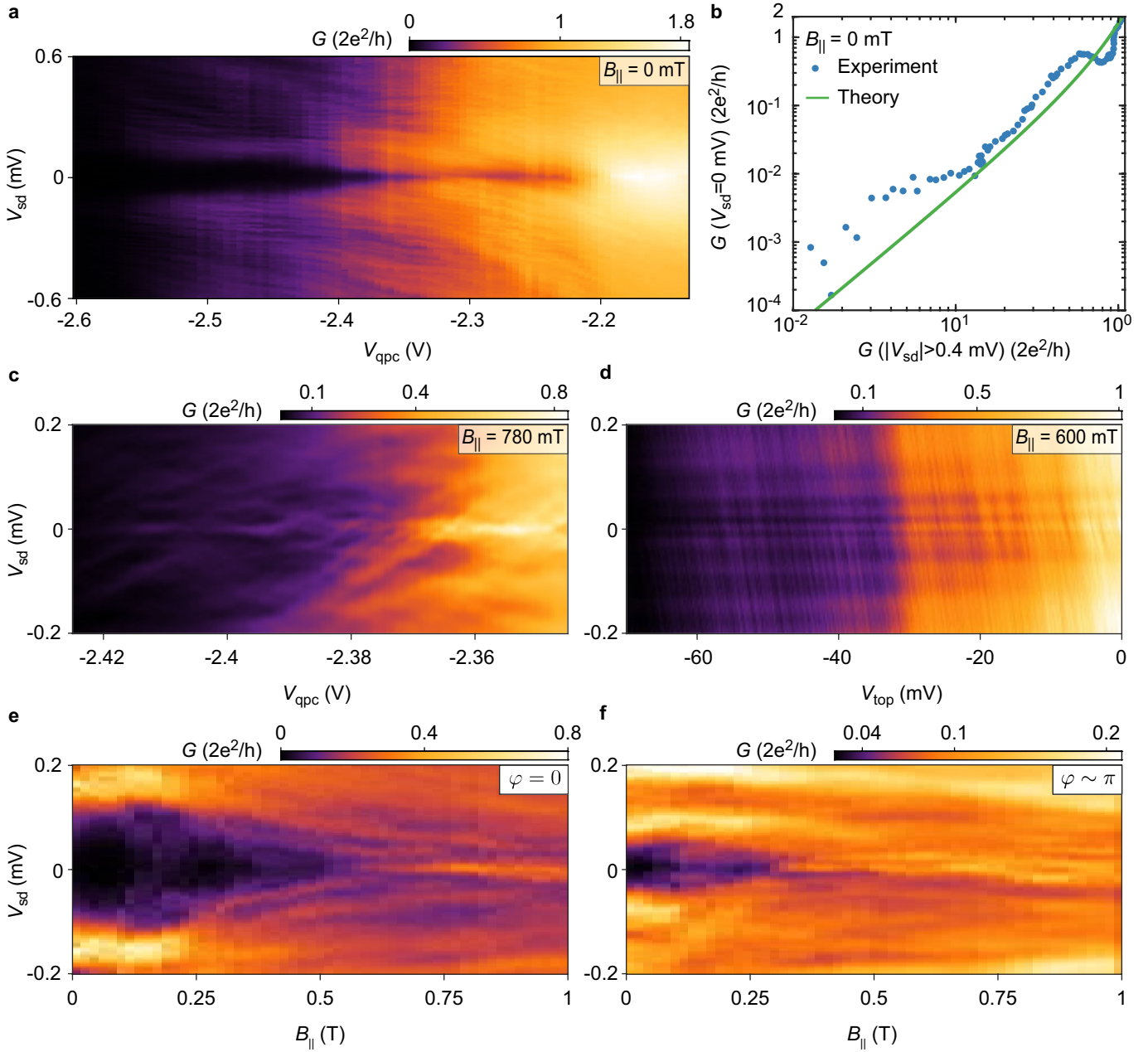
**Extended Data Fig. 2 | Non-symmetric device spectra.** Calculated topological phase diagrams and energy spectra for a left–right asymmetric junction (here the asymmetry is introduced by having  $\Delta_L \neq \Delta_R$ ). As explained in the Methods, the left–right symmetry may be broken by disorder<sup>27,28</sup>, different geometric sizes of the superconducting leads, or different coupling of the 2DEG to the superconductors on the two sides of the junctions. **a**, Topological phase diagram as a function of  $E_Z$  and  $\mu$  for  $\varphi = 0, \pi$ , calculated from the tight-binding Hamiltonian for JJ1 with infinite length (see Methods). **b**, Topological phase diagram as a function of  $E_Z$  and  $\varphi$  for different values of  $\mu$ , as indicated by the horizontal ticks in **a**. The diagrams were calculated for a junction with  $W_1 = 80$  nm,  $W_{S1} = 160$  nm, left-induced gap  $\Delta_L = 150$   $\mu$ eV, right-induced gap  $\Delta_R = 100$   $\mu$ eV and  $\alpha = 100$  meV  $\text{\AA}$ . **c–g**, Calculated energy spectra as a function of  $\varphi$  for different values of the Zeeman energy. The spectra were

obtained for the same parameters used in **a** and **b**, except for  $L_1 = 1.6$   $\mu$ m. Note that the gap for the fine-tuned chemical potential  $\mu = 79.25$  meV, which closes at  $\varphi = \pi$  and  $E_Z = 0$  for a left–right symmetric junction (see Extended Data Fig. 1a, c), now becomes non-zero, and is approximately  $|\Delta_L - \Delta_R|$ . As a result, the topological transition for  $\varphi = \pi$  occurs at finite Zeeman field. For the chosen parameters, the system undergoes a topological transition at  $E_Z = 0.02$  meV for  $\varphi = \pi$  and at  $E_Z = 0.1$  meV for  $\varphi = 0$ . The lowest subgap states are shown in red and indicate two Majorana zero modes at the edges of the junction in the topological regime. The behaviour of the calculated Majorana modes is qualitatively consistent with that of the observed zero-bias peaks in tunnelling conductance. **h, i**, Probability density  $|\Psi|^2$  of the Majorana wavefunction calculated as a function of the spatial directions  $x$  and  $y$  in JJ1 for  $E_Z = 0.13$  meV and  $\varphi = 0, \pi$ .



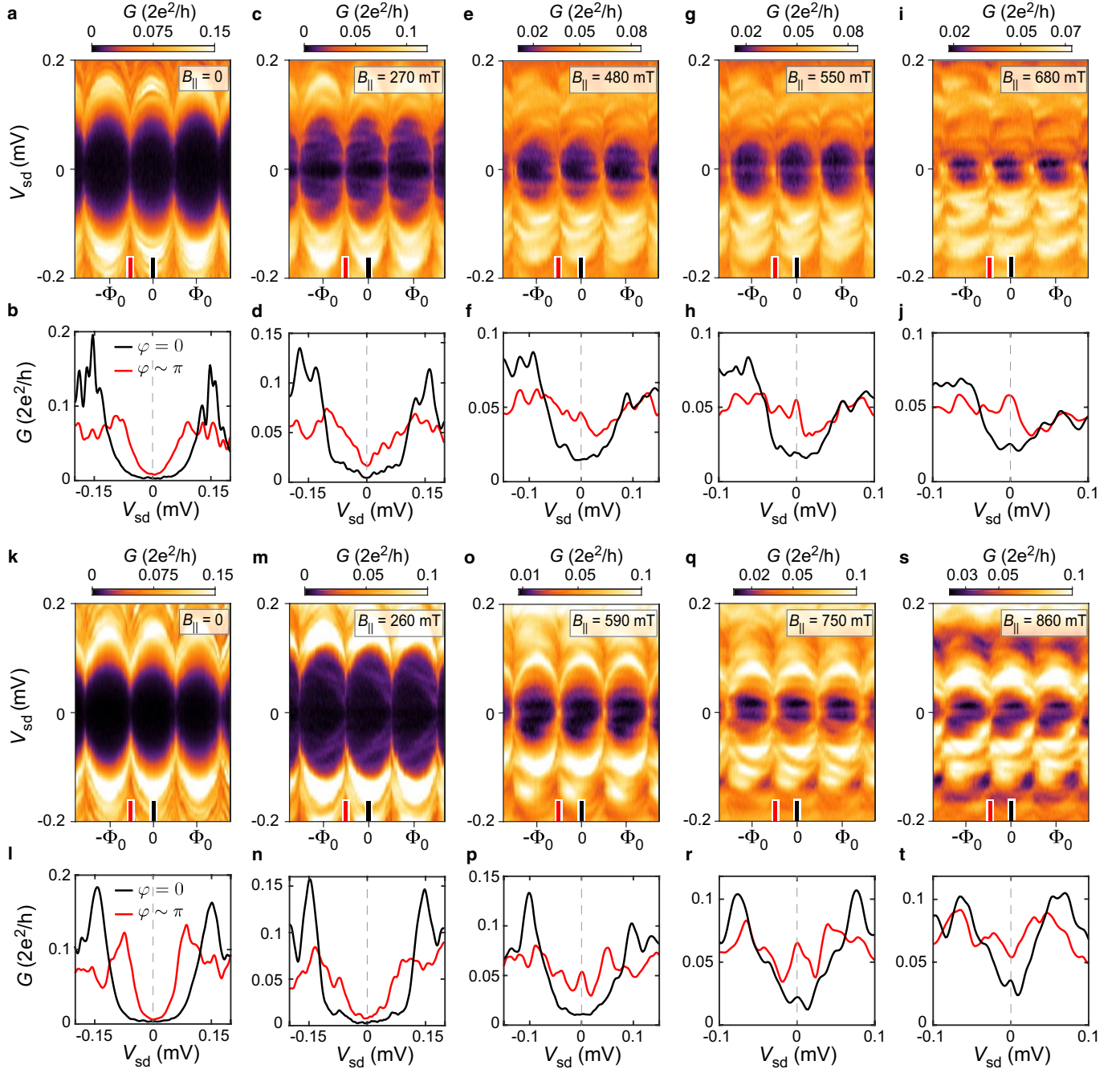
**Extended Data Fig. 3 | Transport spectroscopy in transverse field for device 1.** a–h, Differential conductance  $G$  as a function of the magnetic flux  $\Phi$  threading the SQUID loop and source–drain bias,  $V_{sd}$ , measured

at different values of the transverse magnetic field  $B_t$  (applied in plane orthogonally to the junction) in device 1. Several ABSs enter the gap without sticking to zero energy. The induced gap collapses at  $B_t \approx 360$  mT.



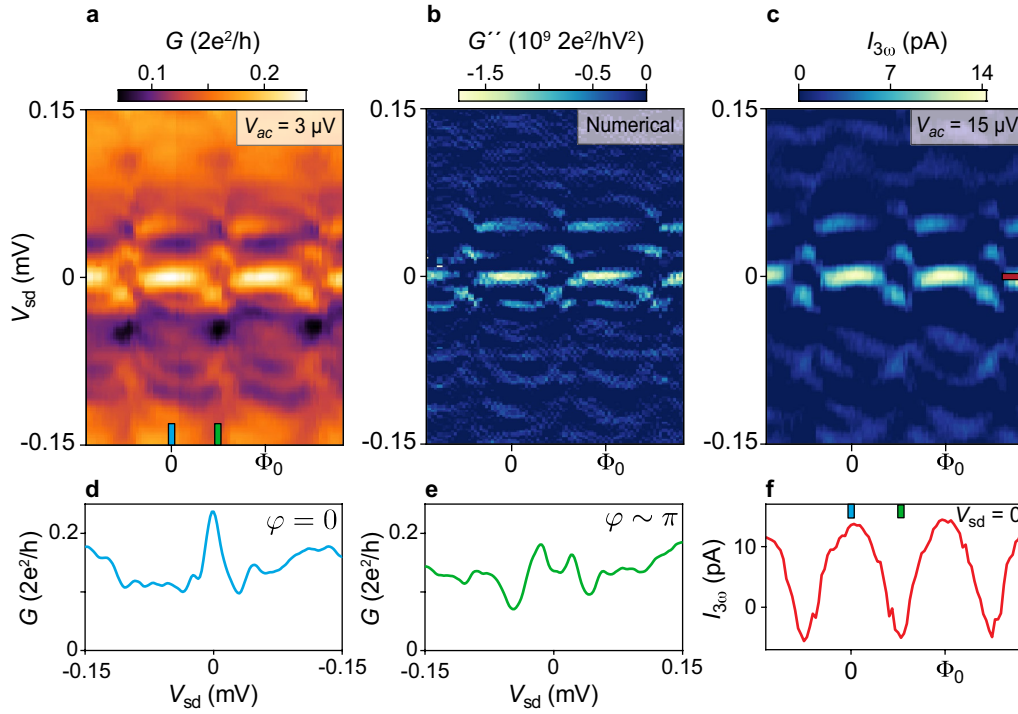
**Extended Data Fig. 4 | Quantum point contact characterization and stability of the zero-bias peak.** **a**,  $G$  as a function of  $V_{sd}$  and QPC voltage  $V_{qpc}$  at zero field in device 1. **b**, Differential conductance at zero source-drain bias,  $G(V_{sd} = 0 \text{ mV})$ , versus averaged differential conductance at finite source-drain bias,  $G(|V_{sd}| > 0.4 \text{ mV})$ . The green line is the theoretically predicted conductance in an Andreev-enhanced QPC,  $G_S = 2G_0 \frac{G_N^2}{(2G_0 - G_N)^2}$  (ref. <sup>38</sup>), where  $G_S$  is the sub-gap conductance,  $G_N$  is the above-gap conductance and  $G_0 = 2e^2/h$  is the quantum of conductance. No fitting parameters have been used. **c**,  $G$  as a function of  $V_{sd}$  and  $V_{qpc}$  at

parallel field  $B_{||} = 780 \text{ mT}$  and  $\varphi \approx 0.8\pi$  for gate voltages  $V_1 = -110 \text{ mV}$  and  $V_{top} = -35 \text{ mV}$ . **d**,  $G$  as a function of  $V_{sd}$  and  $V_{top}$  at  $B_{||} = 600 \text{ mT}$  and  $\varphi \approx 0$  for  $V_1 = -118.5 \text{ mV}$  and  $V_{qpc} = -2.366 \text{ mV}$ . In both **c** and **d**, the ZBP is robust against variation of the above-gap conductance of about one order of magnitude. **e**, **f**,  $G$  as a function of  $V_{sd}$  and  $B_{||}$ , for different values of  $\varphi$  in device 1. The plots have been reconstructed from measurements similar to those shown in Fig. 2 of the main text. For  $\varphi \approx \pi$ , a ZBP forms at  $B_{||} = 0.35 \text{ T}$ , whereas for  $\varphi = 0$  it appears at  $B_{||} = 575 \text{ mT}$ . The ZBP at  $\varphi \approx \pi$  oscillates and moves away from zero energy as the field is increased.



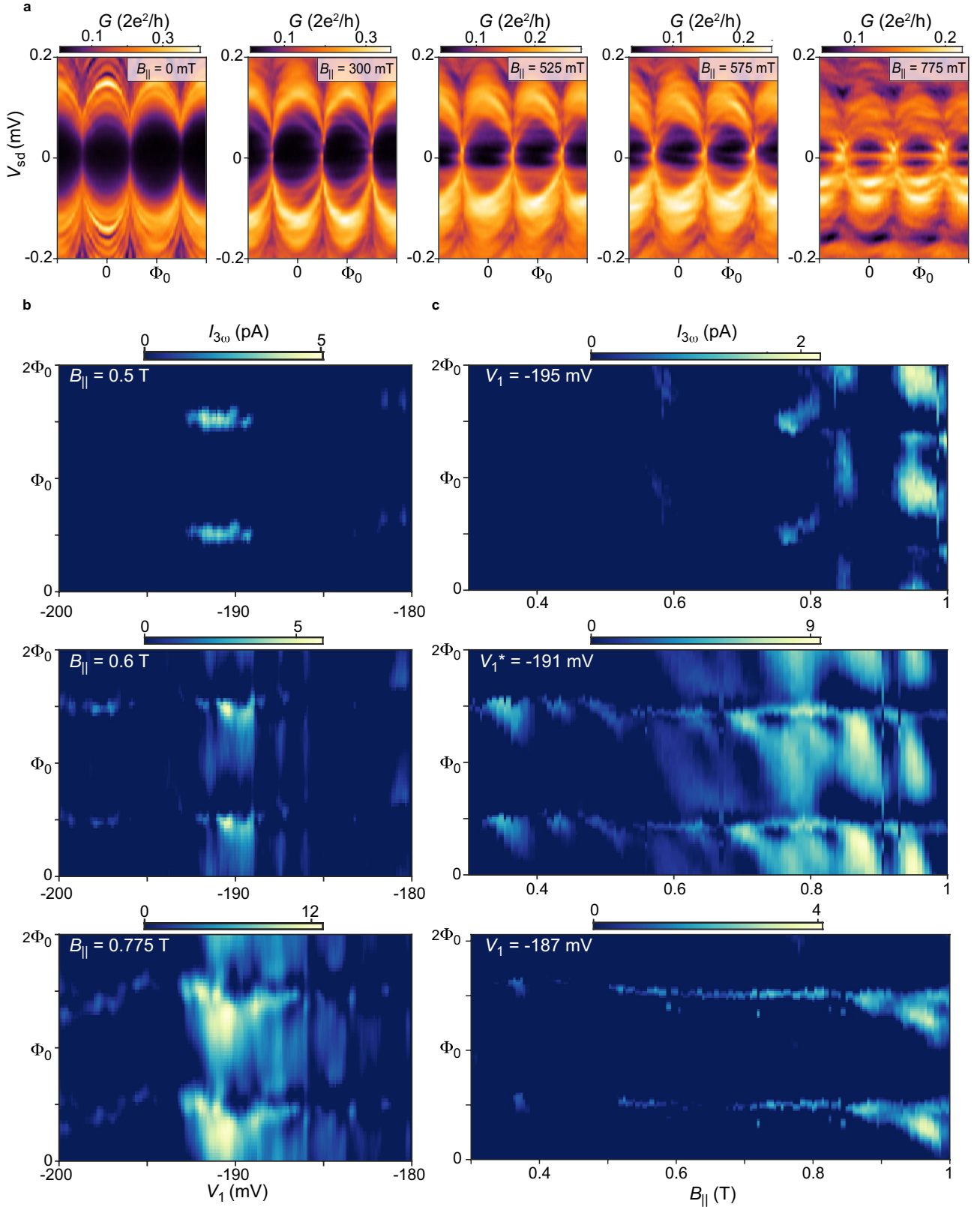
**Extended Data Fig. 5 | Tunnelling spectroscopy at lower tunnelling transmission in devices 1 and 2.** **a–j**, Results obtained for device 1. **k–t**, Results obtained for device 2. The devices were intended to be lithographically identical. **a, c, e, g, i**,  $G$  as a function of  $\Phi$  threading the SQUID loop and  $V_{sd}$  measured at different values of  $B_{||}$  in device 1 ( $W_1 = 80$  nm). The QPC was tuned to reduce the above-gap conductance by a factor of about 3 with respect to the one measured in the regime presented in the main text. At zero field, the sub-gap conductance is

suppressed. Colour extrema have been saturated. **b, d, f, h, j**, Conductance line cuts versus  $V_{sd}$  taken at  $\varphi = 0, \pi$ , as indicated by red and black ticks in **a, c, e, g, i**. The grey dashed lines indicate  $V_{sd} = 0$ . **k, m, o, q, s**,  $G$  as a function of  $\Phi$  threading the SQUID loop and  $V_{sd}$  measured at different values of  $B_{||}$  in device 2 ( $W_1 = 80$  nm). Colour extrema have been saturated. **l, n, p, r, t**, Conductance line cuts versus  $V_{sd}$  taken at phase bias  $\varphi = 0, \pi$ , as indicated by red and black ticks in **k, m, o, q, s**. The grey dashed lines indicate  $V_{sd} = 0$ .



**Extended Data Fig. 6 | Measurement of the third harmonic of the current.** **a**,  $G$  as a function of  $V_{sd}$  and  $\Phi$  at  $B_{||} = 850$  mT measured with an excitation amplitude  $V_{ac} = 3 \mu V$  in device 1. **b**, Numerical second derivative of the conductance  $G''(V_{sd}) = (\partial^2 G / \partial V^2)|_{V_{sd}}$  as a function of  $V_{sd}$  and  $\Phi$  calculated from the data shown in **a**. **c**, Third harmonic of the current  $I_{3\omega}$  versus  $V_{sd}$  and  $\Phi$  measured by the lock-in amplifier using an excitation  $V_{ac} = 15 \mu V$ , as explained in the Methods. To increase the signal-to-noise ratio, the amplitude of the excitation has been chosen to be

greater than the temperature-limited full-width at half-maximum of a Lorentzian feature, that is,  $V_{ac} \approx 3.5 k_B T$ , where  $k_B$  is the Boltzmann constant and  $T \approx 40$  mK is the electron temperature in our devices. Most of the features present in **b** are reproduced in **c**. **d**, **e**, Line cuts of  $G$  as a function of  $V_{sd}$  taken at  $\varphi = 0, \pi$  as indicated by the ticks in **a**. **f**,  $I_{3\omega}(V_{sd} = 0)$  as a function of  $\Phi$ : a positive value of  $I_{3\omega}(V_{sd} = 0)$  indicates a ZBP in  $G$ . See Methods for further details.

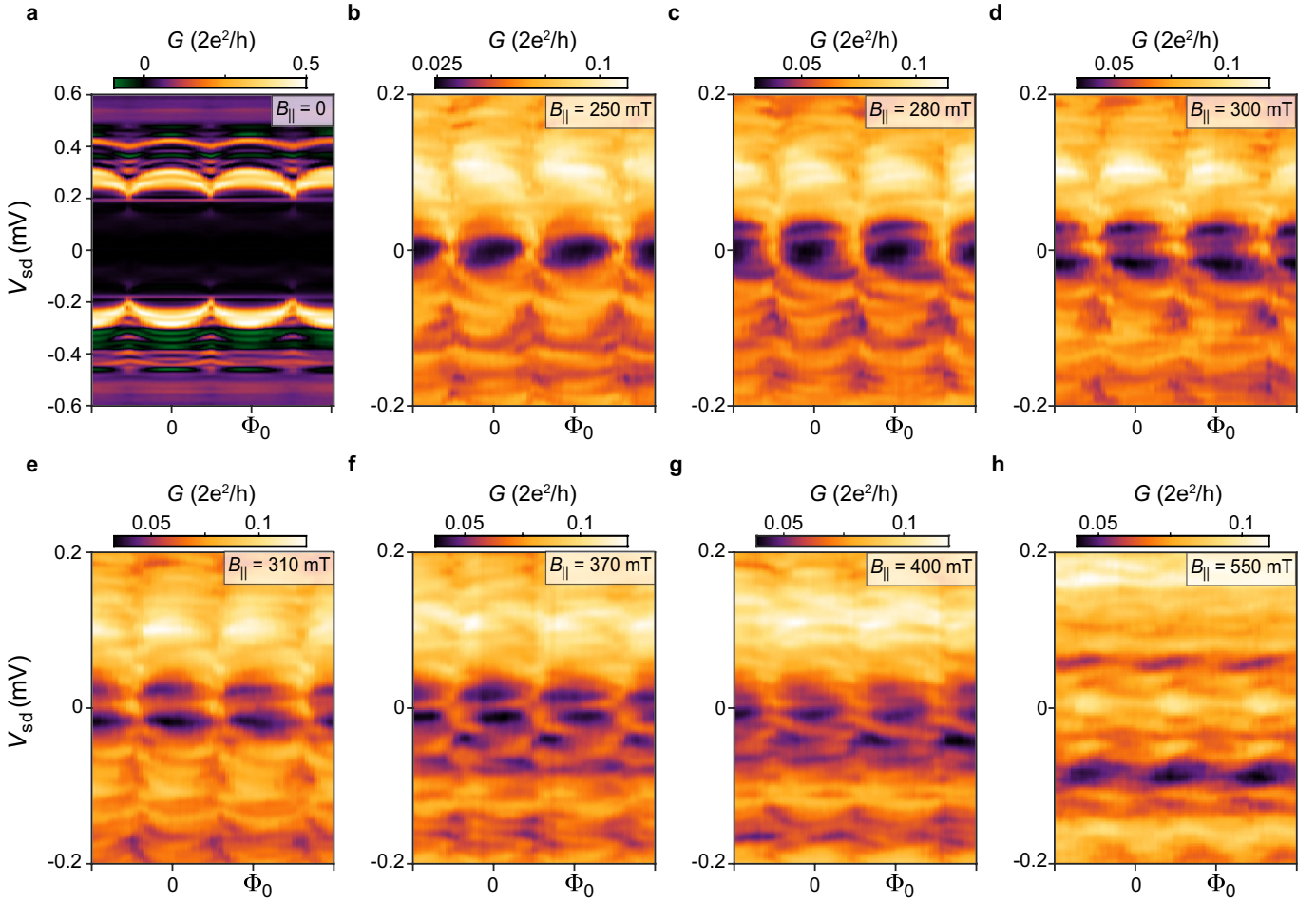


**Extended Data Fig. 7 | Zero-bias peak stability in device 2 ( $W_1 = 80$  nm).**

**a,**  $G$  as a function of  $\Phi$  threading the SQUID loop and  $V_{sd}$  measured at different values of  $B_{||}$  in device 2 at  $V_1 = -191$  mV. **b,** Third harmonic of the current  $I_{3\omega}(V_{sd} = 0)$  measured by the lock-in amplifier at zero bias as a function of  $V_1$  and  $\Phi$  for different values of  $B_{||}$ .  $I_{3\omega}(V_{sd} = 0) \propto -G''(V_{sd} = 0) = -(\partial^2 G / \partial V^2)|_{V_{sd}=0}$ , as shown in the Methods and Extended Data Fig. 6.

A positive value of  $I_{3\omega}(V_{sd} = 0)$  corresponds to a ZBP in conductance as a function of  $V_{sd}$ . As  $B_{||}$  is increased, the ZBP expands in phase and in  $V_1$

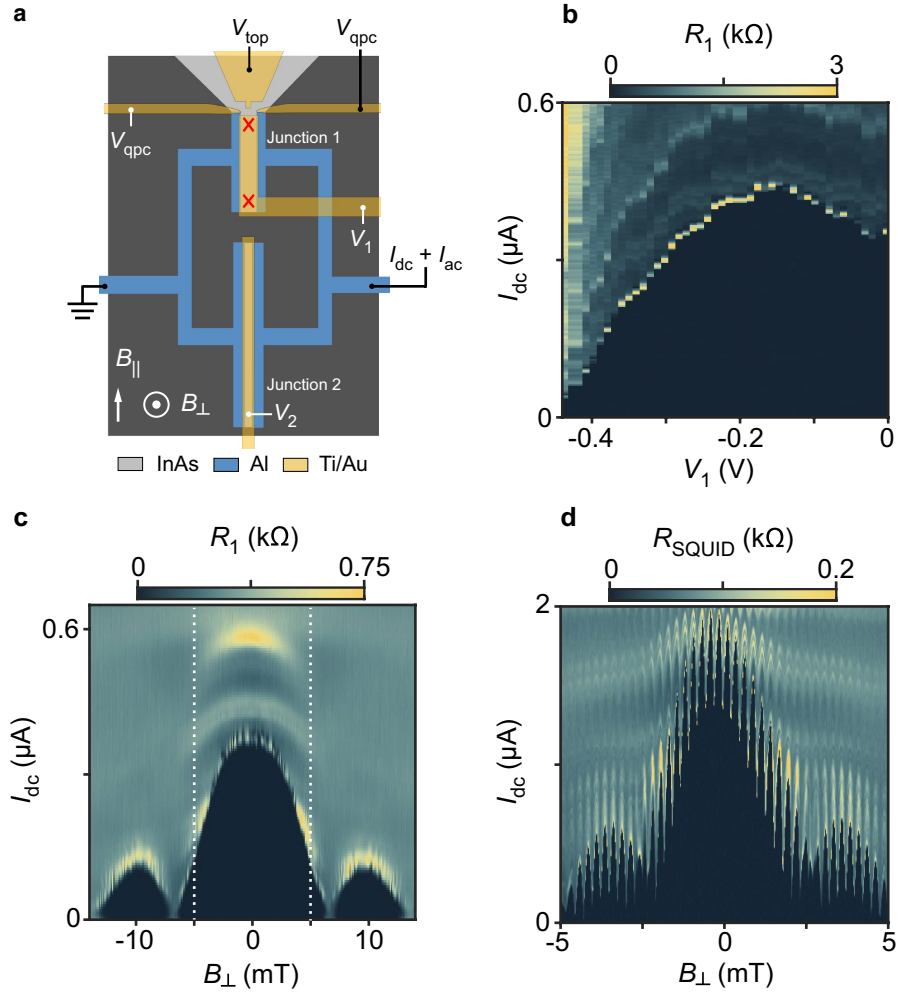
range, consistent to what is observed in Fig. 3 of the main text for device 1. **c,**  $I_{3\omega}(V_{sd} = 0)$  measured by the lock-in amplifier at zero bias as a function of  $B_{||}$  and  $\Phi$  for different values of  $V_1$ . A positive value of  $I_{3\omega}(V_{sd} = 0)$  corresponds to a ZBP in conductance as a function of  $V_{sd}$ . The critical field at which the ZBP first appear is minimized at  $\varphi \approx \pi$ . The behaviour of the ZBP is tuned by  $V_1$  and is qualitatively consistent with the topological phase diagrams shown in Extended Data Fig. 2a, b.



**Extended Data Fig. 8 | Tunnelling spectroscopy in device 3 ( $W_1 = 120$  nm).**

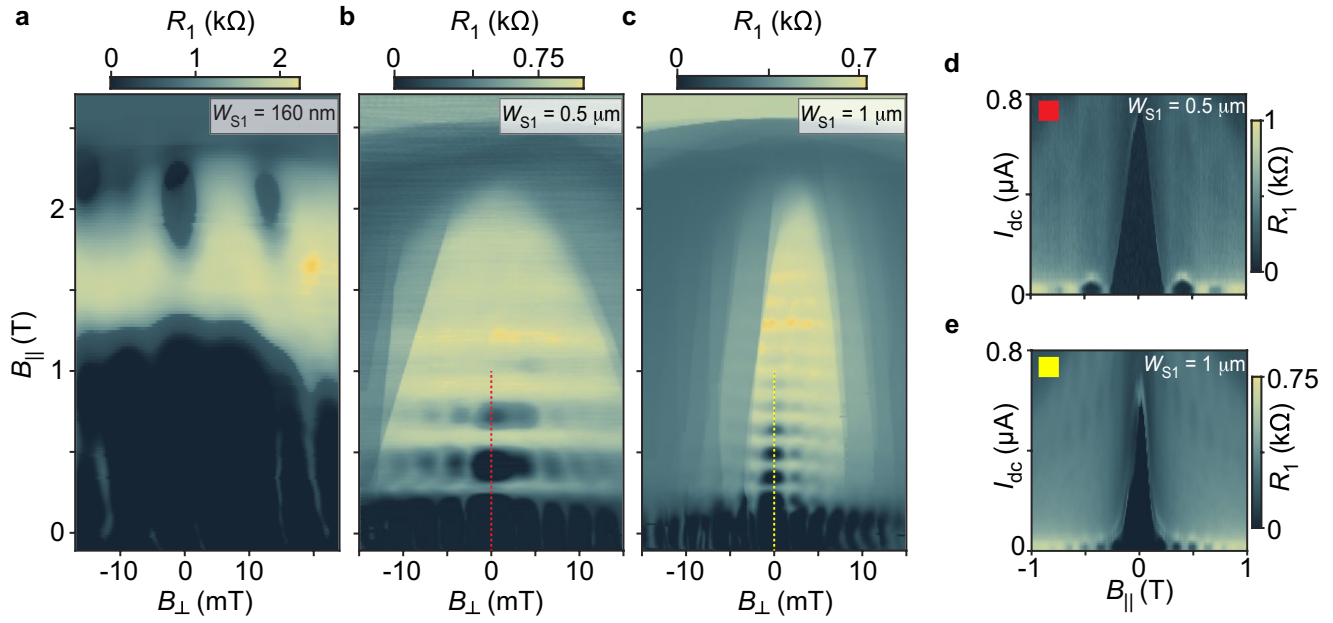
**a–h**,  $G$  as a function of  $\Phi$  and  $V_{sd}$  measured at different values of  $B_{||}$  in device 3 ( $W_1 = 120$  nm). In this device, spectroscopy was performed with a QPC forming a tunnel barrier between the top edge of JJ1 and a wide planar Al lead, following the approach of refs <sup>6,7</sup>. At  $B_{||} = 0$ , the superconducting probe generates a flux-independent gap  $\Delta_{probe}^* \approx 200 \mu\text{eV}$  added to the junction gap  $\Delta \approx 100 \mu\text{eV}$ , together with the characteristic features of negative differential conductance, as visible in **a**. When a moderate parallel field is applied, the superconducting gap below the superconducting plane softens, creating a finite density of states at zero

energy. This feature allows the Al plane to be used as an effective normal lead that can probe discrete states close to zero energy in the junction. At  $B_{||} = 250$  mT, we can see a complete phase modulation of  $\Delta$ , indicating that the Al plane gap is already soft (see **b**). As the field is increased, two ABSs move towards zero energy, forming a ZBP first localized at phase bias  $\varphi \approx \pi$  and then extending up to  $\varphi = 0$ , as shown in **c–f**. At higher fields, the induced gap collapses (**g, h**). The lower value of  $\Delta$  and critical field compared to that observed in devices 1 and 2 are presumably due to the larger width of the junction.



**Extended Data Fig. 9 | Behaviour of the Josephson critical current at  $B_{\parallel} = 0$ .** **a**, To investigate the behaviour of the Josephson current in our device, we measured the differential resistance  $R = dV/dI$  of the SQUID with a conventional four-probe technique by applying an a.c. bias  $I_{\text{ac}} < 5$  nA, superimposed on a variable d.c. bias  $I_{\text{dc}}$ , to one of the superconducting leads of the interferometer. During these measurements the QPC was pinched off at  $V_{\text{qpc}} = -5$  V. The Josephson critical current of JJ1 can be measured independently by pinching off JJ2. **b**, Differential resistance  $R_1$  of JJ1 as a function of the  $I_{\text{dc}}$  and  $V_1$  measured in device 2. The region of zero resistance indicates that a dissipationless Josephson current due to Cooper pair transport is flowing through the junction.

**c**,  $R_1$  as a function of  $I_{\text{dc}}$  and the out-of-plane field  $B_{\perp}$  displaying a characteristic Fraunhofer pattern, with a periodicity compatible with the area of JJ1  $W_1 \times L_1 \approx 0.13 \mu\text{m}^2$ . For both the measurements displayed in **a** and **c**, JJ2 was pinched off by setting the gate voltage  $V_2 = -1.5$  V. **d**, When JJ2 was open ( $V_2 = 0$ ), the differential resistance of the SQUID  $R_{\text{SQUID}}$  showed periodic oscillations (periodicity of  $250 \mu\text{T}$ , consistent with the area of the superconducting loop,  $\sim 8 \mu\text{m}^2$ ) superimposed to the Fraunhofer patterns of both junctions. The ratio between the critical currents of the junctions at zero field is extracted from the average value of the SQUID critical current and the semi-amplitude of the SQUID oscillations, resulting in  $I_{c,2}(0)/I_{c,1}(0) = 5.2$ .



**Extended Data Fig. 10 | Josephson current revival in parallel field.**

**a–c**, Differential resistance  $R_1$  of JJ1 as a function of  $B_{\perp}$  and  $B_{\parallel}$  measured in devices 2, 6 and 7 for  $I_{dc} = 0$  and  $I_{ac} = 5$  nA. All the devices are characterized by width  $W_1 = 80$  nm and length  $L_1 = 1.6 \mu\text{m}$ , while the width of the superconducting leads  $W_{S1}$  (see Fig. 1a) is varied. Device 2 is characterized by  $W_{S1} = 160$  nm, device 6 has  $W_{S1} = 500$  nm and device 7  $W_{S1} = 1 \mu\text{m}$ . In the case of  $W_{S1} = 160$  nm (a), JJ1 becomes resistive at  $B_{\parallel} \approx 1.1$  T, and a supercurrent revival is observed above 2 T. The normal state transition of the epitaxial Al occurs at  $B_{\parallel} \approx 2.4$  T, where the junction

resistance reaches a value of about 1 k $\Omega$  without any magnetic-field dependence. When  $W_{S1}$  is increased, the supercurrent revivals occur at lower values of  $B_{\parallel}$  and show an evident periodicity of about 300 mT and about 150 mT for  $W_{S1} = 500$  nm (b) and  $W_{S1} = 1 \mu\text{m}$  (c), respectively. **d, e**,  $R_1$  as a function of  $I_{dc}$  and  $B_{\parallel}$  measured in devices 6 and 7 for  $B_{\perp} = 0$ , as shown by the dashed lines in b and c. The Josephson current shows a clear Fraunhofer pattern due to orbital effects of the in-plane field penetrating the proximitized 2DEG below the Al leads<sup>10</sup>. The measurements were performed with the QPC and junction 2 pinched off.